

# A Total-Power Radiometer Front End in a 0.25- $\mu\text{m}$ BiCMOS Technology With Low $1/f$ -Corner

Satoshi Malotau, *Student Member, IEEE*, Masoud Babaie, *Member, IEEE*, and Marco Spirito, *Member, IEEE*

**Abstract**—This paper describes the analysis, design, and characterization of a high-sensitivity millimeter-wave total-power radiometer front-end integrated into a 0.25- $\mu\text{m}$  SiGe:C BiCMOS technology. This prototype is composed of a two cascode stage low-noise amplifier (LNA) and a voltage-driven common-emitter square-law detector. The LNA is interfaced to the detector through a low transformation ratio (i.e., high-impedance node) to achieve an efficient wideband signal transfer. The front end achieves both a low  $1/f$ -noise corner and a low noise-equivalent power (NEP) by combining a large area, high resistive value load resistor together with a minimum size heterojunction bipolar transistor. At 56 GHz and optimum bias, the prototype provides a 61-MV/W responsivity which combined with a 194-nV/ $\sqrt{\text{Hz}}$  white noise level result in a 3.2-fW/ $\sqrt{\text{Hz}}$  NEP when the input power is modulated with a frequency above the 30-Hz flicker noise corner. The achieved 3-dB NEP bandwidth is 6 GHz.

**Index Terms**—Direct detection, flicker noise, low-noise amplifier (LNA), millimeter-wave (mm-wave), radiometer, square-law detector.

## I. INTRODUCTION

PASSIVE millimeter-wave (mm-wave) radiometers provide the ability to detect objects in optically obscured conditions with a spot size resolution, determined by their lowest operating frequency, capable of providing images to support various applications, i.e., surveillance, concealed threats, and navigation support systems [1]. In all these applications, the ability of a radiometer system to distinguish between small temperature variations, or in other words provide high-temperature resolution, is paramount in achieving image quality or object detection.

Passive radiometers operate with limited signal-to-noise-ratio as they aim to detect the relatively weak signal composed of the thermal radiation of objects in the presence of background noise. These systems are, however, of interest, as they feature low-power consumption and complexity, small silicon footprints, and are not restricted to specific frequency bands by spectrum regulations. These key characteristics of passive radiometers together with the absence of any high-frequency on-chip signal/clock distribution make them amenable for low-power integration in large focal plane array architectures [2] [3]. With the increase in the maximum

oscillation frequency of silicon-based devices, i.e., CMOS [4] and BiCMOS [5], full monolithic implementations of passive radiometers have become possible [6]–[18], which allow, employing the various devices and components available in silicon platforms, to co-integrate control, calibration, and digital circuitry.

Nevertheless, to provide a useful output signal passive radiometers require a high level of low-noise amplification to sufficiently reduce the impact of the detector noise, (i.e., in [6], for a noise figure of 10 dB, the required gain level is close to 25 dB). This is often achieved through stage peaking and high-Q matching networks, between the stages and the detector. This approach tends to limit the bandwidth of these systems (both the gain and minimum noise bandwidth), thus reducing the amount of thermal energy down-converted by the radiometer. Moreover, the losses associated with the mm-wave switches used to modulate the signal beyond the  $1/f$ -noise corner, add to the receiver noise temperature and therefore reduce the system's temperature resolution. In this contribution, the low-noise amplifier (LNA) is directly interfaced to the detector through a non-50- $\Omega$  interface to achieve a more efficient signal transfer between these two blocks. Furthermore, the use of an optimized large area load resistor in the detector results in a low flicker noise corner. This, in principle, allows the system to operate without the use of a Dicke switch to periodically calibrate the radiometer [19], or the need for bias switching [20].

The organization of this paper is as follows. Section II describes the figures of merit of a radiometer and provides an analysis of detector-limited radiometers to describe how low-temperature resolution can be achieved. The conclusions of this analysis are then used to guide the design of a radiometer prototype and illustrate the context in which the front end described in this paper operates. Section III covers the circuit design of both the LNA and the square-law detector and their silicon integration. Section IV describes the experimental characterization and presents the measurement results of the entire radiometer and compares its performance to the state of the art.

## II. RADIOMETER SYSTEMS

The main figures of merits for a direct detection front end are its  $1/f$ -noise corner frequency and its noise-equivalent power (NEP). The corner frequency is important as it limits the available stable integration time [21], while NEP relates the amount of power needed within the front-end's bandwidth to

Manuscript received December 20, 2016; revised April 8, 2017; accepted May 4, 2017. Date of publication June 12, 2017; date of current version August 22, 2017. This paper was approved by Guest Editor Sorin P. Voinigescu. (*Corresponding author: Satoshi Malotau.*)

The authors are with the Delft University of Technology, 2628 CD Delft, The Netherlands (e.s.malotau@tudelft.nl).

Color versions of one or more of the figures in this paper are available online at <http://ieeexplore.ieee.org>.

Digital Object Identifier 10.1109/JSSC.2017.2705659

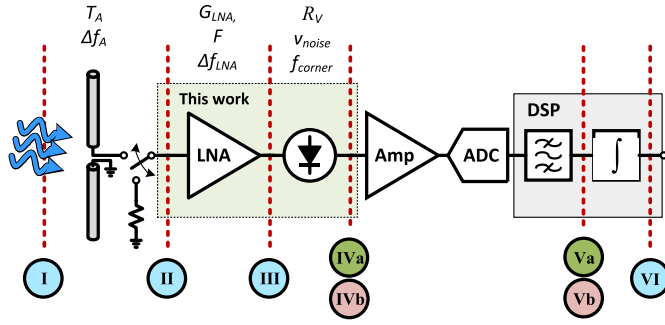


Fig. 1. Simplified block diagram of a pre-amplified Dicke switch passive radiometer.

obtain a signal that is equal to its noise floor (i.e.,  $\text{SNR} = 1$ ), and thereby sets the required integration time for a desired temperature resolution [6], and the NEP is given by

$$\text{NEP} = \frac{v_n}{R_V} \quad (1)$$

where  $v_n$  is the noise voltage at the output of the detector and  $R_V$  is the responsivity, which expresses the efficiency with which the radiometer is able to convert a given RF power  $P_{\text{RF}}$  at the input to a linearly proportional dc voltage shift at its output  $\Delta v_{\text{out}}$  and is defined as

$$R_V = \frac{\Delta v_{\text{out}}}{P_{\text{RF}}}. \quad (2)$$

The signal processing chain of a passive Dicke radiometer [22] is given in Fig. 1, and the power spectral densities (PSDs) that correspond to each of the inter-stage nodes (I–VI) are drawn in Fig. 2. It is assumed for simplicity's sake, that all bandwidths of the front-end stages are aligned and that all stages are matched. For the initial part of this analysis, the reader should ignore the switch and thus, also the bandpass filter shown in the DSP of Fig. 1 should for now be replaced with a low-pass filter. PSD-I gives the power available at the antenna terminals, as predicted by Planck's law. The power emitted in the mm-waves by objects at ambient temperatures, complies with the Rayleigh–Jean approximation and thus increases with the square of the frequency [23]. PSD-II shows the power available at the output of the antenna terminal across its bandwidth. At the output of the antenna, the available power can be approximated by

$$P_{\text{(II)}} = k_B T_A \Delta f_{\text{RF}} \quad (3)$$

where  $k_B$  is the Boltzmann's constant,  $T_A$  is the antenna temperature, and  $\Delta f_{\text{RF}}$  is the effective front-end bandwidth. The signal is then amplified by the LNA. The noise power at the output of the LNA can be estimated by

$$P_{\text{(III)}} = k_B (T_A + T_{\text{LNA}}) G_{\text{LNA}} \Delta f_{\text{RF}} \quad (4)$$

where  $G_{\text{LNA}}$  is the LNA gain, and  $T_{\text{LNA}}$  is the LNAs input referred equivalent noise temperature. The squaring operation of the detector then results in PSD-IVa (as explained in [1]),

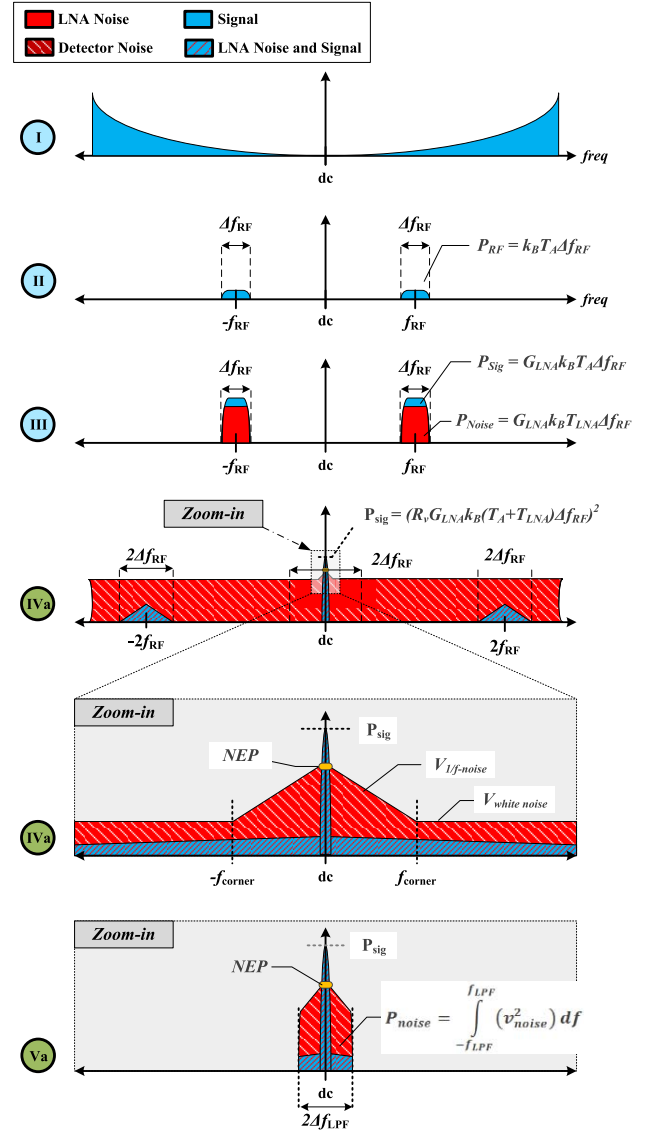


Fig. 2. Simplified illustrations describing the PSDs found at various nodes of the radiometer scheme block of Fig. 1 with a non-modulated RF input signal.

which is described by

$$P_{\text{(IVa)}}(f) = k_B^2 T_{\text{sys}}^2 \left[ \int_{-\infty}^{\infty} |H(f)|^2 df \right]^2 \delta(f) + 2k_B^2 T_{\text{sys}}^2 \int_{-\infty}^{\infty} |H(f)|^2 |H(f' - f)|^2 df \quad (5)$$

where  $H(f)$  is the combined transfer function of all stages preceding the detector, and  $T_{\text{sys}}$  is the sum of  $T_A$  and  $T_{\text{LNA}}$ . The first term represents a dc signal while the second term represents the convolution of the input power spectrum, which results in three spectral densities. One centered around dc, and the other two at the double of the front-end center frequency (i.e.,  $-2f_{\text{RF}}$  and  $2f_{\text{RF}}$ ) each with decreasing magnitudes (i.e., sketched triangular shape) over double the system bandwidth ( $2\Delta f_{\text{RF}}$ ). Now, as this paper covers a detector-limited radiometer, the noise generated by the detector is added to the output. In silicon-based technologies, this noise is expected to dominate the output spectrum close to dc [6]–[18]. Further, we assume that the bandwidth of the low-pass

filter ( $\Delta f_{\text{LPF}}$ ) is significantly lower than that of the RF front end ( $\Delta f_{\text{LPF}} \ll \Delta f_{\text{RF}}$ ) so that the PSD close to dc resembles the version of PSD-IVa (zoomed-in), and is described by

$$P_{\text{IVa}} = R_V^2 G_{\text{LNA}}^2 k_B^2 T_{\text{sys}}^2 \Delta f_{\text{RF}}^2 + R_V^2 G_{\text{LNA}}^2 k_B^2 T_{\text{sys}}^2 \Delta f_{\text{RF}} \Delta f_{\text{LPF}} + \int_{-f_{\text{LPF}}}^{+f_{\text{LPF}}} v_{n,\text{det.}}^2(f) df \quad (6)$$

where  $v_{n,\text{det.}}^2(f)$  is added to account for the detector noise (i.e., flicker, shot and thermal noise). Due to the addition of the  $1/f$ -noise the latter PSD is no longer constant across frequency, and is therefore represented as an integral across the low-pass filter's bandwidth (PSD-Va). All the square terms in (6) result from the detector output being a voltage that needs to be squared to again represent a power. The first term in (6) provides the mean value of the output signal due to the front-end equivalent noise temperature, and is the desired signal. The second term represents the output fluctuations, which can be assumed flat in a narrowband around dc [24]. When the signal of interest  $\Delta T$  is a small perturbation over the antenna temperature  $T_A$ , the signal and noise at the detector output can be defined as shown in

$$P_s = R_V^2 G_{\text{LNA}}^2 k_B^2 \Delta T^2 \Delta f_{\text{RF}}^2 \quad (7)$$

$$P_n = R_V^2 G_{\text{LNA}}^2 k_B^2 T_{\text{sys}}^2 \Delta f_{\text{RF}} \Delta f_{\text{LPF}} + \int_{-f_{\text{LPF}}}^{+f_{\text{LPF}}} v_{n,\text{det.}}^2(f) df \quad (8)$$

$$\text{SNR} = \frac{P_s}{P_n} = \frac{R_V^2 G_{\text{LNA}}^2 k_B^2 \Delta T^2 \Delta f_{\text{RF}}^2}{R_V^2 G_{\text{LNA}}^2 k_B^2 T_{\text{sys}}^2 \Delta f_{\text{RF}} \Delta f_{\text{LPF}} + \int_{-f_{\text{LPF}}}^{+f_{\text{LPF}}} v_{n,\text{det.}}^2(f) df} \quad (9)$$

The minimum sensitivity is found when the  $\text{SNR} = 1$ , in this case, we can rewrite (9) in terms of the minimum detectable temperature  $\Delta T$  as shown in

$$\Delta T = \sqrt{T_{\text{sys}}^2 \frac{\Delta f_{\text{LPF}}}{\Delta f_{\text{RF}}} + \frac{1}{R_V^2 G_{\text{LNA}}^2 k_B^2 \Delta f_{\text{RF}}^2} \int_{-f_{\text{LPF}}}^{+f_{\text{LPF}}} v_{n,\text{det.}}^2(f) df} \quad (10)$$

The consequence of directly down converting the high-frequency input signal is that the output is a dc term that lies within the flicker noise region, severely limiting the achievable temperature resolution and nullifying the use of an integrator to improve the SNR [21]. When the high-frequency input signal is modulated (50% duty cycle) before it reaches the detector, e.g., with an RF switch in the case considered by Fig. 1, the output signal is up-converted (from dc) to the modulation frequency as described by PSD-IVb (see Fig. 3).

By modulating with a frequency above the  $1/f$ -noise corner value, the output signal can then be placed in the white noise region. The penalty is that now the signal power is halved [22], and it is spread across multiple harmonics that compose the pulsed signal. Nevertheless, this loss tends to be favorably offset by the reduced contribution of the flicker noise. Considering the first harmonic as the wanted signal,

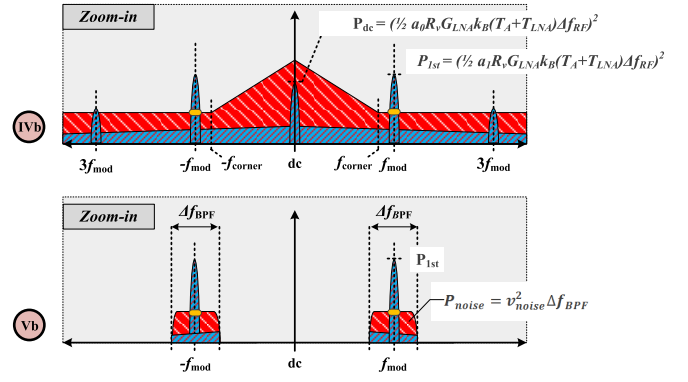


Fig. 3. Simplified illustrations of the PSDs found at the inter-stage nodes of the radiometer of Fig. 1 with a modulated RF input signal.

the output power and noise contributions are, respectively, expressed by

$$P_s = \frac{1}{2} \alpha_1^2 R_V^2 G_{\text{LNA}}^2 k_B^2 \Delta T^2 \Delta f_{\text{RF}}^2 \quad (11)$$

and

$$P_n = \frac{1}{4} \alpha_1^2 R_V^2 G_{\text{LNA}}^2 k_B^2 T_{\text{sys}}^2 \Delta f_{\text{RF}} \Delta f_{\text{BPF}} + v_{n,\text{det.}}^2 \Delta f_{\text{BPF}} \quad (12)$$

where  $\alpha_1$  is the first Fourier coefficient of the pulsed detector output, and  $v_{n,\text{det.}}^2$  the detector's white noise level. The constant power level of the noise (PSD-Vb), in the up-converted region, simplifies the integral in (10) and allows an integrator to improve the SNR over a given acquisition time [21]. Under these conditions, the temperature resolution can be expressed by

$$\Delta T = \sqrt{T_{\text{sys}}^2 \frac{\Delta f_{\text{BPF}}}{\Delta f_{\text{RF}}} + \frac{v_{n,\text{det.}}^2 \Delta f_{\text{BPF}}}{\frac{1}{2} \alpha_1^2 R_V^2 G_{\text{LNA}}^2 k_B^2 \Delta f_{\text{RF}}^2}} \quad (13)$$

where  $\Delta f_{\text{BPF}}$  is the bandwidth of the bandpass filter. Equation (13) describes the available temperature resolution if the final output resembles a pulse train. It should be noted that (13) ignores any gain variations in the combined transfer function of the stages preceding the detector, which can significantly degrade the achievable temperature resolution. This is commonly solved by periodically calibrating against a known noise source using a Dicke switch after the antenna (see Fig. 1) [4], [19]. In radiometer systems exhibiting a low flicker noise, this is, however, less critical. Note that integration/averaging can still be employed to improve SNR when a technologies exhibiting  $1/f^a$ , with  $a$  lower than 1 is used [25]. Furthermore, gain variation can, to some extent, be compensated by adding thermal monitoring circuitry [26], adding dummy/reference receiver chains (high thermal coupling and matching in silicon), or an on-chip noise source for calibration [22], [27], which could all be integrated, in radiometers array architectures using silicon technologies.

### III. LNA AND DETECTOR BLOCKS: DESIGN AND CHARACTERIZATION

The simplified circuit schematics of the LNA and the square-law detector that constitute the radiometer front end

are shown in Fig. 4. The LNA of two cascode stages given in Fig. 4(a) and a common-emitter square-law detector is shown in Fig. 4(b).

#### A. Technology

The radiometer front end is designed using a 0.25- $\mu\text{m}$  SiGe:C BiCMOS process (NXP's Gen 8 [28]–[30]) which provides a peak  $f_T/f_{\text{max}}$  of 200/180 GHz and a dc current gain  $\beta$  of  $\sim 2000$ . This technology is optimized to serve as a cost-effective alternative to GaAs technologies for application in high-performance RF circuitry [31]. The library features high-voltage (HV) device and low-voltage (LV) devices, which are available in a number of characterized layouts, optimized for different applications. Two of these layouts are employed in the design of the radiometer. The LNA uses LV devices with the layout that offers the highest  $\beta$  and  $f_T$  thereby allowing a lower minimum noise figure with a given gain. Instead, the square-law detector uses an HV device with a layout that can be sized smaller than the one utilized in the LNA. The HV allows the  $Q_5$  to operate with the 2.5-V supply at its collector allowing it to remain in forward active mode across a broader range of powers, while the smaller feature size provides higher responsivity to a given amount of current. The back end of line consists of three standard lower metals and two thick top metals of 2 and 3  $\mu\text{m}$ , respectively. The process is further complimented with an array of p-type and n-type diffusion and poly-silicon resistors as well as N-well-, poly-poly- and metal-insulator-metal (MIM) capacitors. The MIM capacitor utilizes a dedicated stack on the top of the first thick metal layer, consisting of a  $\text{Ta}_2\text{O}_5$  dielectric and a TiN top plate. It provides a capacitance density of 5 fF/ $\mu\text{m}^2$  with self-resonance frequencies of several hundreds of GHz. Shallow and deep trench isolation are used to isolate both devices and circuit blocks. The process is implemented on a 200- $\Omega/\text{cm}$  substrate to reduce substrate losses.

#### B. Low-Noise Amplifier

The LNA amplifies the incoming mm-wave signal to overcome the noise contribution of the detector while minimizing its own contribution to system's noise temperature. For passive radiometers which collect broadband radiation of thermal objects, an additional requirement is a large bandwidth. The input device ( $Q_1$ ) of the LNA, is biased at peak  $f_T$  ( $\approx 5 \text{ mA}/\mu\text{m}^2$ ) to optimize both noise and gain. Contrary to designs at lower frequencies, optimal noise and gain operation are achieved at the same a point. An explanation for this can be found in the relatively high operating frequency as compared to the available  $f_T$  provided by the technology. This can be illustrated through (14), which provides the minimum noise factor  $F_{\text{min}}$  of a bipolar device in a CE configuration [32]

$$F_{\text{min}} = 1 + \frac{1}{\beta} + \sqrt{2g_m r_B} \sqrt{\left(\frac{1}{\beta} + \frac{f^2}{f_T^2}\right)} \quad (14)$$

where  $g_m$  is the transconductance,  $r_B$  is the base resistance, and  $f_T$  is the cutoff frequency. When operating close to the  $f_T$  of a technology, the term  $f^2/f_T^2$  inside the second square-root

tends to dominate, and a bias point which sacrifices  $f_T$  to achieve a lower  $NF_{\text{min}}$  (as done at lower frequencies [33]) can no longer be chosen. To obtain a simultaneous noise and impedance match, the input device  $Q_1$  is inductively degenerated with  $L_1$  (106 pH) and  $L_{\text{par}}$  ( $\approx 10$  pH) [34]. Note that the parasitic inductance  $L_{\text{par}}$  [see Fig. 4(a)] between the emitter of  $Q_1$  and the on-chip ground plane, is realized using a 8- $\mu\text{m}$  line in the top metal that is directly connected to the on-chip ground plane consisting of a maximum metal density mesh constructed using all available metal layer. This connection on its own provides the required inductance value for the degeneration, thus no additional inductor is needed. The ground mesh employing all metal layers, is used throughout the layout, with the exception for the RF sensitive areas, where the mesh consist of only the lowest metal layer at maximum density.

The devices of the second stage ( $Q_3$  and  $Q_4$ ) are sized smaller than in the previous stage to keep their parasitic capacitances low. These devices were again chosen for maximum  $f_T$  (3.6 mA/ $\mu\text{m}^2$ ) to provide the needed gain at the desired frequency of operation. Load inductor  $L_4$  (140 pH) is not tuned toward a 50  $\Omega$ , but to maximize the voltage swing when terminated by the input impedance of the detector Fig. 3(b). The matching between the two cascode stages is realized through an LC-network consisting of  $C_1$  and  $L_3$ , which simultaneously provides the dc block and the easy bias path for the second stage [35]. Cascode stages are employed for their higher reverse isolation, gain, and bandwidth [36], and the base of the cascode devices are directly decoupled through a small value resistor to prevent any oscillations. The stability of the complete LNA and both stages individually is verified across frequency by calculating the  $\mu$ -parameter of each stage using the S-parameters obtained when both input and output are terminated to 50- $\Omega$ . (i.e.,  $\mu(f)$  larger than 1).

All mm-wave interconnections, critical supply nodes, and the layout geometries of the inductors and the metal-oxide-metal (MOM) capacitor ( $C_1$ ) are custom designed considering [37] and [38], using 2.5-D EM simulations from Keysight MoMentum. The custom design of  $C_1$  was necessary because the library MIM capacitor could not be sized sufficiently small to provide the 25 fF needed for the match. It is implemented as an MOM capacitor by interdigitating the two top metals to ease routing (bridging the distance between the stages), and the capacitance estimation through EM simulation was deemed to be more accurate for large structures.

The performance of the second stage could have been improved in terms of gain and bandwidth by the introduction of an inter-cascode matching inductor. But is omitted because the required value (80 pH) would significantly impact the overall layout area ( $\pm 0.8 \text{ pH}/\mu\text{m}$ ).

The values of load inductors  $L_2$  and  $L_4$  are chosen to obtain a frequency offset between the gain peaks of different stages to increase the LNA's overall bandwidth, as shown in Fig. 5. When terminated with the input impedance of the detector, the two stages provide a gain of 25 dB at 63 GHz. The parasitically tuned gain (i.e., adding extra capacitance at the MIM detector interface after comparing it with measured data) curve is also added. This deduced gain curve predicts that

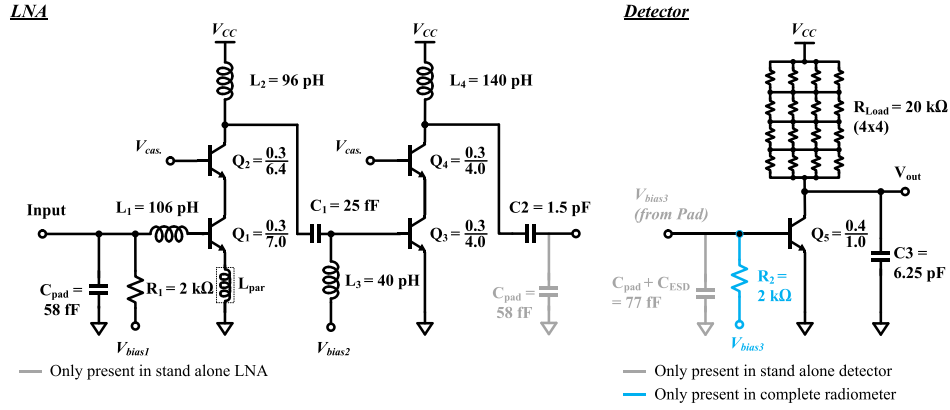


Fig. 4. Simplified circuit schematic of (a) LNA and (b) square-law detector.

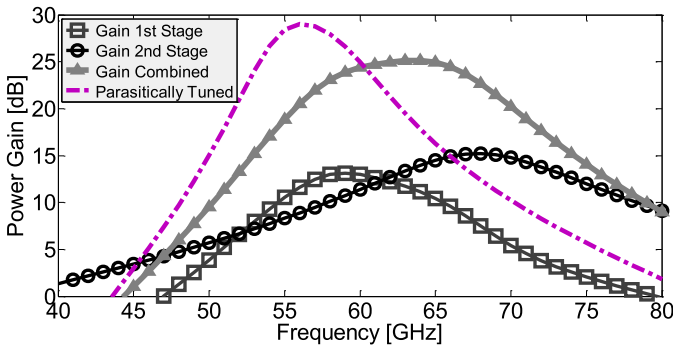


Fig. 5. Simulated power gain of LNA when terminated with the square-law detector.

the radiometer embedded LNA (i.e., loaded with the input impedance of the detector) produces 28 dB gain at 56 with 5-GHz bandwidth. A micrograph of the stand-alone LNA is presented in Fig. 6, and the simulated versus measured S-parameters and noise figure are given in Fig. 7, exhibiting a fair agreement. The measured  $S_{21}$  and noise figure of the LNA at 56 GHz (50- $\Omega$  termination) were 21 dB and 5.3 dB, respectively, while drawing 18 mA from a 2.5-V supply. It is worth mentioning that the reduced small-signal gain and peaking frequency shown in Fig. 5 compared to the curve presented in Fig. 7 originate from the 50  $\Omega$  termination, set by the wafer probes, and the larger capacitance of the output pad compared to the detector transistor.

### C. Square-Law Detector

To achieve decently low NEP for the square-law detector [Fig. 4(b)] a good tradeoff between responsivity and output noise is required. The detector employs a minimum size HV device  $Q_5$  in CE configuration, a large area load resistor, and capacitance  $C_3$  which provides a low-impedance path to short the fundamental and harmonics to prevent any unwanted RF variations across the terminals of  $Q_5$  [6] and concurrently forms a low-pass filter with  $R_{load}$  that limits the noise bandwidth at the output of the detector to around 1.2 MHz [13]. The CE topology is chosen for its higher responsivity, for operation below  $f_T$  [39], when compared to diode connected, or emitter follower counterparts. Furthermore having a simpler layout

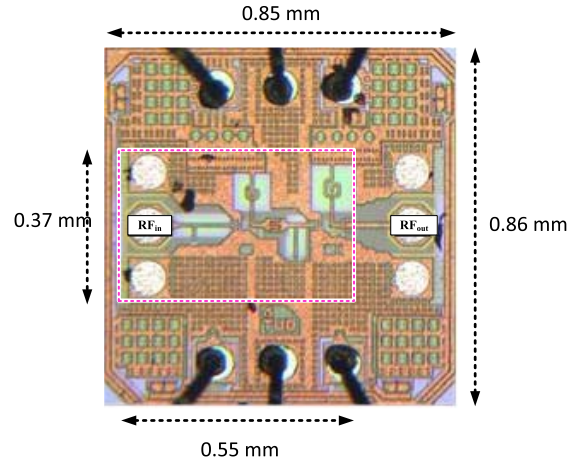


Fig. 6. Micrograph of stand-alone LNA.

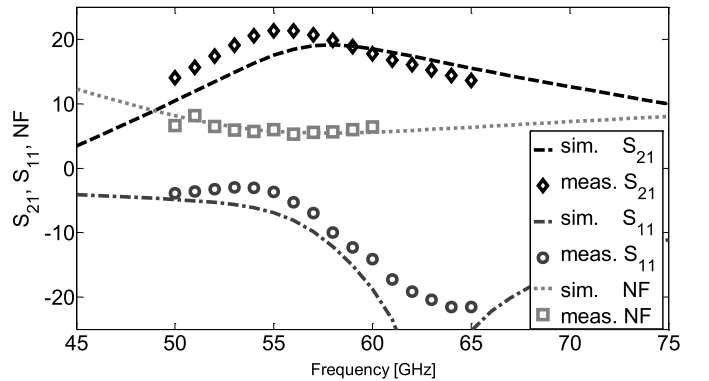


Fig. 7. Simulated and measured performance of the stand-alone LNA when terminated with 50  $\Omega$ .

than the common-base configuration [40]. Transistor  $Q_5$  is minimum size to provide higher responsivity [6].

The square-law detector provides responsivity through the use of  $Q_5$ 's non-linear transfer characteristic (i.e., exponential) at low bias voltages. When excited by small signals, the non-linear transfer provides a squaring function that generates a shift in collector current, by pulling this current across the load resistor  $R_{load}$ . The magnitude of the dc voltage shift due to the second-harmonic component of the input signal can be estimated by employing the Taylor approximation around the



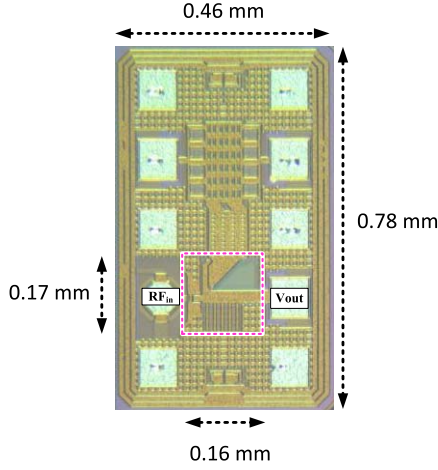


Fig. 8. Micrograph stand-alone CE detector.

chosen bias point, under the conditions that  $V_{in} < V_T$  [11]

$$\Delta v_{out} \approx \eta I_C \frac{1}{4} \left( \frac{V_{in}}{V_T} \right)^2 R_{load} \quad (15)$$

where  $I_s$  is the reverse saturation current of the base-emitter diode,  $V_{in}$  is the small-signal excitation across the base-emitter junction,  $V_T$  is the thermal voltage ( $k_B T/q$ ), and  $\eta$  gives the efficiency of the signal transfer between the LNA and detector (described in the following section). As can be gathered from (15), the response of the detector can be improved by enhancing the efficiency of the signal transfer to the detector (increasing  $V_{in}$ ) and by increasing the collector current or  $R_{load}$ . Note that (15) is only valid under the condition that  $Q_5$  operates in forward active mode and its non-linear transfer characteristic is not compromised (linearized) by the presence of the  $R_{load}$ . As a consequence the possible responsivity improvement through both  $R_{load}$  and  $I_C$  are bounded.

The PSD at the output of the detector is composed of shot-, thermal-, and  $1/f$ -noise. For now assuming operation in the white noise limited region ( $1/f$ -noise ignored) and combining the output noise together with (15) into (1), as in [11], one obtains the following relation for the NEP

$$NEP = \frac{\sqrt{v_n^2(f_{LF})}}{R_o} = \frac{1}{\eta} \sqrt{\frac{2q}{I_C} + \frac{4k_B T}{I_C^2 R_{load}}}. \quad (16)$$

Here, it should again be stated that both the increase of  $I_C$  and  $R_{load}$  are bounded by the need of ensuring a non-linear transfer characteristic. The transition between the shot- and thermal-noise can be found where the two terms under the square become equal. Consequently, the tradeoff between the two noises occurs when

$$I_C R_{load} \approx \frac{4k_B T}{2q} \approx 2V_T. \quad (17)$$

Note that the flicker noise in general increases with the dc current [41]. Hence, the design features a preference for low current and a high resistance. When considering the  $1/f$  noise performance, on first approximation it would be expected that the HBT  $Q_5$  would be the main source of flicker noise in the square-law detector. It is, however, already noted

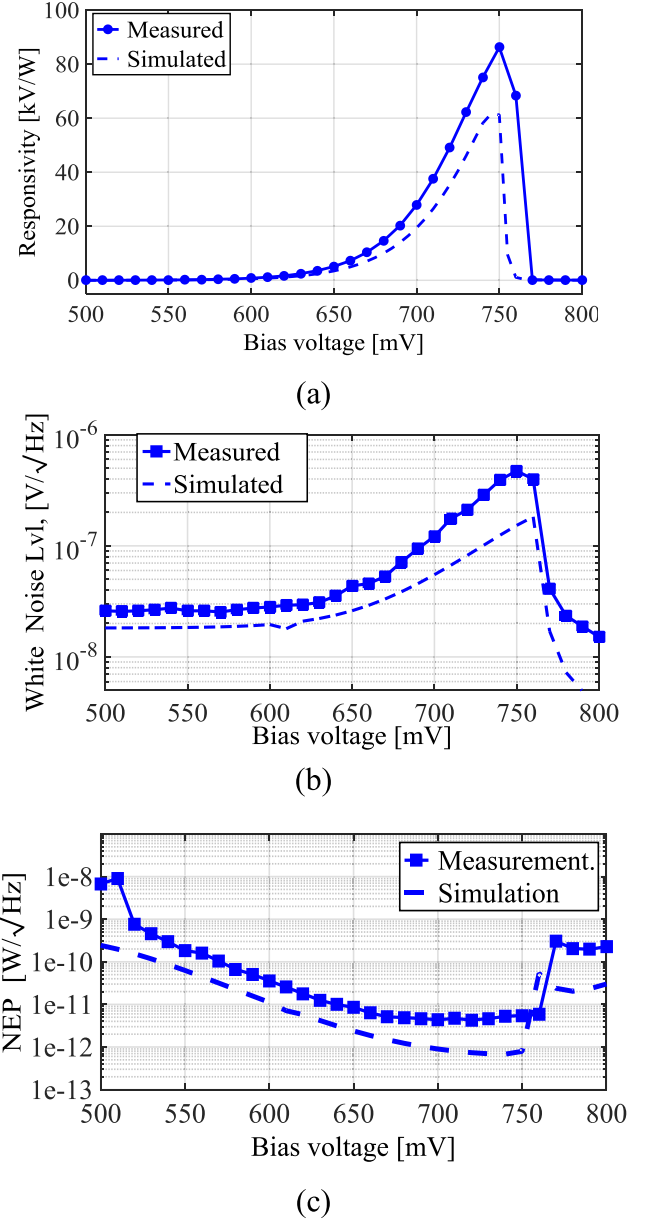


Fig. 9. Simulated and measured (a) responsivity, (b) white noise level, and (c) NEP versus bias voltage of the ESD protected stand-alone square-law detector.

in [6] that the load resistor can significantly degrade expected flicker noise performance if left unattended. Simulations using the resistors in the library confirmed this and subsequent evaluation resistors showed that the base poly-silicon resistor (p-type in NPN's) generated the least amount of flicker noise for a given amount of current. This result is consistent with the theory presented in [42], which relates the  $1/f$ -noise to the random release and emission of charge carriers from traps located between the boundaries of the poly-silicon grains that make up the resistor and predicts p-type resistors to be less noisy. Moreover, [42] provides a simplified equation of their model for designers, that describes the flicker noise  $S_I(f)$

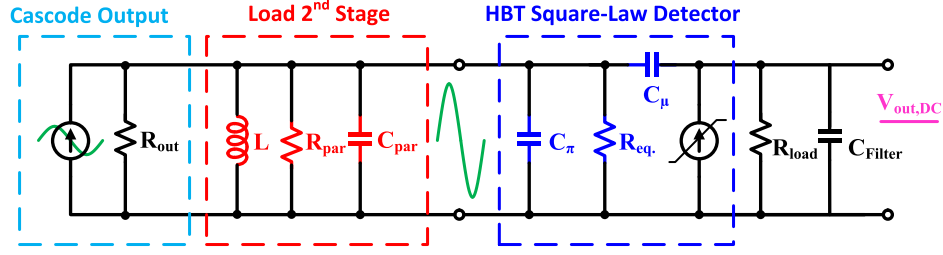


Fig. 10. Simplified equivalent circuit to illustrate optimization of the parallel resonance of the node connecting the LNA to the square-law detector.

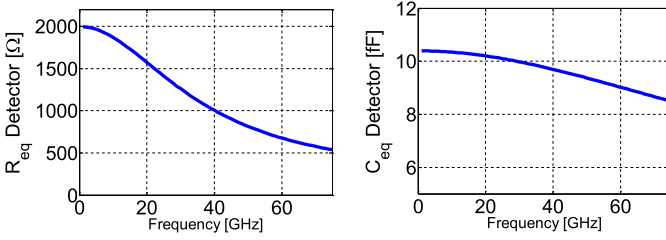


Fig. 11. Simulated equivalent small-signal values for the parallel equivalent (a)  $R_{eq}$  and (b)  $C_{eq}$  of the minimum sized detector HBT  $Q_5$ .

generated by a poly-silicon resistor

$$S_I(f) = \frac{1}{WL} \frac{K_f}{f} I_{dc}^2 \quad (18)$$

where  $W$  and  $L$  are the width and length of the resistor,  $K_f$  is a technology dependent variable (lower for p-type),  $I_{dc}$  is the dc current flowing through the resistor. From this equation, it is concluded that in order to reduce the  $1/f$ -contribution a large area resistor with a low dc current is desirable. Therefore, the physical size of the load resistor is increased to the extent that it would not significantly impact our pad limited area ( $100 \times 100 \mu\text{m}^2$ ), and to conform to the design rule check of the technology, the resistor is implemented  $4 \times 4$  series parallel configurations.

The micrograph of the stand-alone detector is shown in Fig. 8. The input of this stand-alone detector is protected by electrostatic discharge (ESD) diodes connected under the pad to prevent damage during fabrication and assembly [see Fig. 4(b)]. The measured and simulated responsivity and noise at the output of the stand-alone detector versus bias are shown in Fig. 9(a) and (b), respectively. The responsivity is calculated using the actual power entering the detector (i.e., after accounting for the reflection losses), and thus represents the intrinsic responsivity of the detector. The NEP computed from the responsivity and noise using (2), is shown in Fig. 9(c). Note that the NEP continuously decreases with increasing current, until  $Q_5$  is pulled out of forward active mode due to the voltage drop over  $R_{load}$ . For this stand alone detector the minimum NEP is found when biased at a low dc current (i.e.,  $5.6 \mu\text{A}$ ).

#### D. LNA-Square-Law Detector Interface

As can be observed from (15), the dc voltage shift realized at the output of  $Q_5$  is proportional to the voltage swing generated by a given RF input power through  $\eta$ . In order to maximize the voltage swing at the input of the detector, the load inductance

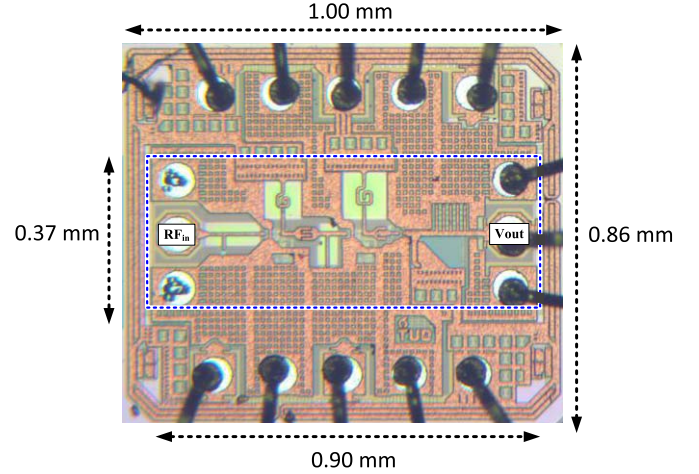


Fig. 12. Micrograph of the complete radiometer front end.

of the second stage of the LNA ( $L_4$ ) is tuned to resonate with both the input capacitance of the detector and the output capacitance of the cascode, respectively,  $C_{par}$  and  $C_{eq}$  in the equivalent LNA detector interface circuit, as shown in Fig. 10. In this situation, the output resistance of the cascode ( $R_{out}$ ) and the input impedance of the detector ( $R_{eq}$ ) need to be kept as large as possible (i.e., optimizing the transistor size and bias) to avoid loading the resonant tank. The simulated input equivalent resistance ( $R_{eq}$ ) and capacitance ( $C_{eq} \approx C_{\pi} \parallel C_{\mu}$ ) of the detector  $Q_5$  at the optimal biasing as found in measurements of the embedded detector are shown in Fig. 11. The detectors in [18] and [43] increase their effective input impedance through the use of a quarter-wave transmission line to isolate the collector of  $Q_5$  from the ac ground at the detector output. However, this technique is not used here to conserve area and because the feed through  $C_{\mu}$  of  $Q_5$  (parallel capacitance to ac ground) could be neglected due to the small device size. The additional benefits of maximizing the voltage transfer at the LNA detector interface are: the avoidance of bandwidth limitations (i.e., arising from the transformation ratio from  $R_{out}/R_{eq}$  to  $50 \Omega$ ), insertion losses (generated by the transformation ratio and limited Q-factor of the components), and area consumption of the matching network between the LNA and detector [4].

#### IV. RADIOMETER CHARACTERIZATION

The micrograph of the radiometer front end composed of the LNA and the square-law detector is given in Fig. 12. The size of the die is 1.0 mm by 0.86 mm and the active area

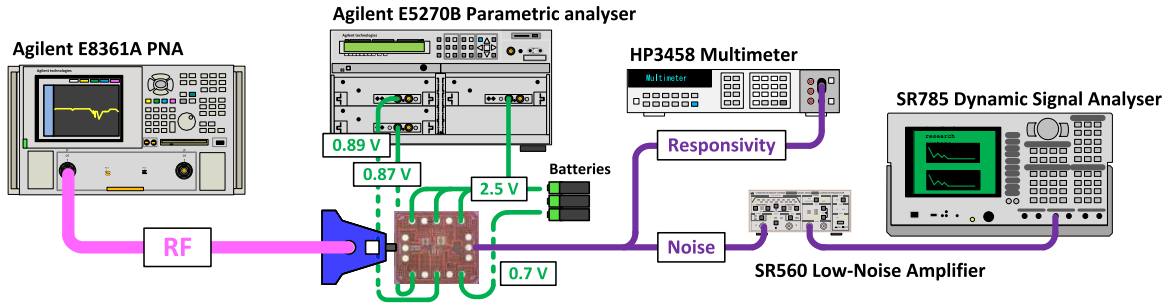


Fig. 13. Measurement setup used for mm-wave and low-frequency characterization of the direct detection radiometer front end.

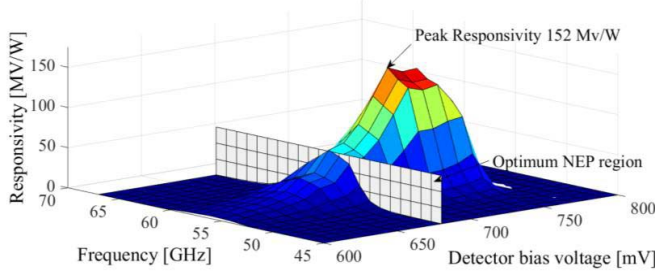


Fig. 14. Measured radiometer responsivity across both frequency and bias with intersecting plane at the empirically found optimum NEP bias voltage of 680 mV.

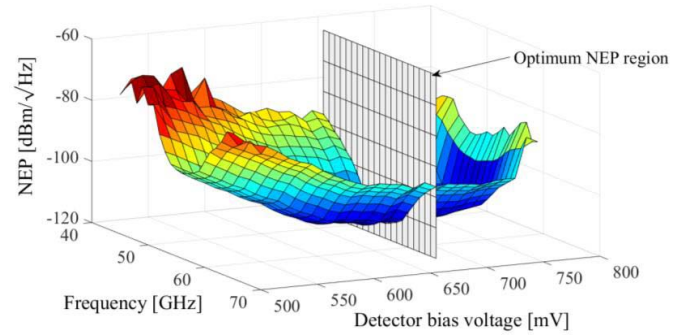


Fig. 15. Measured NEP across detector bias and RF frequency with intersecting plane at the empirically found optimum NEP bias voltage of 680 mV.

occupies  $0.35 \text{ mm}^2$ . In order to allow easy probing at the input, the die is fixed on a test printed circuit board, which simultaneously provides bias connectivity and an access point to the output signal. The measurement setup used in both the high- and low-frequency characterization of the radiometer is given in Fig. 13.

#### A. High-Frequency Measurements

In the responsivity measurement, the RF signal is supplied by an E8361 PNA and delivered to the input pad of the radiometer using a GSG Infinity probe from Cascade Microtech. Meanwhile, the bias voltages are provided by an Agilent E5270B parameter analyzer and an HP3448 multimeter is used to measure the shift in output voltage due to the insertion of RF power at the input. The shift is produced by measuring the output voltage while turning the RF power of the PNA ON and OFF and then computing the difference between the two measured values ( $\Delta v_{\text{out}} = v_{\text{out}}^{\text{RF OFF}} - v_{\text{out}}^{\text{RF ON}}$ ). However, before the actual measurement is done, the mm-wave setup is first vector corrected (using a coaxial port short-open-load and an on-wafer load-reflect-match calibration). After this step, the relation between the power setting of the PNA receiver and the power delivered to the on-wafer environment is derived using a WR-15 HPV8486 diode-based power meter. This method, described in [44], allows calculation of the available power at the probe tips during each individual measurement without any need to disconnect the setup. This vector-based power correction reduces fluctuations in the responsivity measurement across frequency (i.e., often arising from simple scalar calibration approaches), which is important as the responsivity is calculated using the value of the available power according (1). Fig. 14 shows the results

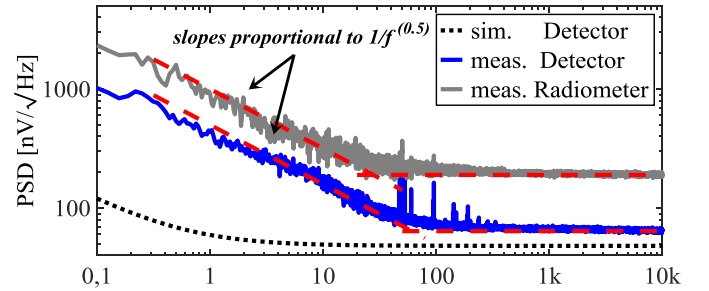


Fig. 16. Measured and simulated PSD at 680 mV.

of this measurement versus both detector bias voltage and RF frequency. One can clearly see a responsivity bulge at the frequencies where the LNA provides gain, and at the bias voltages where the square-law detector has a strong second-order non-linearity. The measured peak responsivity of 152 MV/W is found at 56 GHz and a bias voltage of 720 mV.

#### B. Low-Frequency Measurements

During the low-frequency noise characterization, the bias voltages are provided by tunable batteries and voltage dividers instead of the parameter analyzer. This is done to prevent the injection of supply noise. Also, the multimeter at the output of the device-under-test is replaced by an SR560 low-noise voltage amplifier, which in turn is connected to the SR785 dynamic signal analyzer. This analyzer then measures the output PSD of the detector. Using this configuration, the output PSDs at different bias voltages are collected. The corresponding white noise levels of these PSDs are combined with the previously stated responsivity results using relation



TABLE I  
FRONT-END STATE-OF-THE-ART COMPARISON

Ref	Technology	Front-end Integration	$f_{RF}$ [GHz]	BW [%]	Gain [dB]	NF [dB]	NEP [fW/ $\sqrt{\text{Hz}}$ ]	$R_V$ [MV/W]	$f_{\text{corner}}$ [Hz]	Power [mW]	Area [mm <sup>2</sup> ]
[6]	0.12- $\mu\text{m}$ SiGe BiCMOS	SPDT - 5-stage LNA - Detector	93	21	23	8.0	13	4.4	10 k	34.8	0.40
[7]	65-nm CMOS	SPDT - 5-stage LNA - Detector	86	21	27	6.8	162	0.15	400 k	38.4	0.31
[8]	65-nm CMOS	5-stage LNA – Mixer-Detector	86	11.6	35	8.9	6.1	16.1	30 M	94	2.00
[11]	0.18- $\mu\text{m}$ SiGe BiCMOS	Switch -5-stage LNA – Detector	94	32	30	9.0	20	43	1 M	200	12.5
[12]	0.13- $\mu\text{m}$ SiGe BiCMOS	5-stage LNA - Detector	165	6.1	35	11.0	14	28	<500	95	0.37
[9]	65-nm CMOS	Switch – 5-stage LNA - Detector	140	15	31	8.8	26	1.2	2.5 M	152	0.23
[13]	0.18- $\mu\text{m}$ SiGe BiCMOS	SPDT – 4 stage LNA - Mixer-Detector	96	20.8	40	8.3	8.1	285	40 k	197	2.63
[10]	65-nm CMOS	SPDT- 4 stage LNA- Detector	95	20.1	40	7.6	32	103	10 M	151	1.17
[14]	0.13- $\mu\text{m}$ SiGe BiCMOS	4 stage LNA – Detector #	97.5	21.5	43	11	0.28	800	10 k	225	1.17
[15]	0.13- $\mu\text{m}$ SiGe BiCMOS	Switch – LNA - Detector	92	16.3	-	-	37	27000	-	75	0.32
[17]	0.13- $\mu\text{m}$ SiGe BiCMOS	Switch – LNA - Detector	91	8.8	42	7.5	1.9	166	100 k		3.42
[18]	90-nm SiGe BiCMOS	3 stage -LNA - Detector	136	8.7	36	7.9	1.4	52	160	47.2	0.52
<b>This work</b>	0.25- $\mu\text{m}$ SiGe BiCMOS	2-stage LNA + detector	56	10.7	21*	5.3	3.2	61	30	42.5	0.33

# 4 correlated pixels from a “super” pixel

\* Measured gain with 50-Ohm load (from VNA measurements), the gain when of the radiometer embedded LNA terminated by the detector deduced to be 28 dB as shown in Fig. 5.

(2), to obtain Fig. 15. This figure shows the measured NEP across bias voltage and frequency. As in [36], the NEP remains relatively stable across bias voltage, as both the responsivity and the white noise level are proportional to the collector current of the detector. The lowest NEP is measured at a detector bias voltage of 680 mV. The PSDs found at this bias voltage of the detector, and the PSD of the LNA detector combination is given in Fig. 16. When only the square-law detector is on, the measured white noise level is 66 nV/ $\sqrt{\text{Hz}}$  with a  $\pm 50$  Hz noise corner. When the LNA is added, the white noise level increases to 194 nV/ $\sqrt{\text{Hz}}$  and concurrently the noise corner shifts to 30 Hz. The discrepancy between the simulated and measured  $1/f$ -noise originates from either the discrete components used to set the bias voltages during measurements or the die itself. The outside environment can be eliminated, as the discrepancy persisted during measurements in an anechoic chamber. A cutout across frequency and

at the bias voltage that produced the lowest NEP of both Figs. 14 and 15 is given in Fig. 17. This figure shows that the maximum responsivity at this bias voltage is found to be 61 MV/W, which results in a NEP of 3.2 fW/ $\sqrt{\text{Hz}}$  when combined with the 194 nV/ $\sqrt{\text{Hz}}$  white noise level that would be found with an RF modulation frequency of 100 Hz.

### C. Front-End Results

The results of the radiometer are listed in Table I, which also provides a performance overview of other silicon integrated radiometers published in the literature. The design stands out with its low flicker noise corner at  $\pm 30$  Hz. This result combined with the noise corner achieved in [16] shows the merit of using large area load resistors for flicker noise reduction. The mm-wave performance metrics are more difficult to compare due to the difference in operating frequencies.

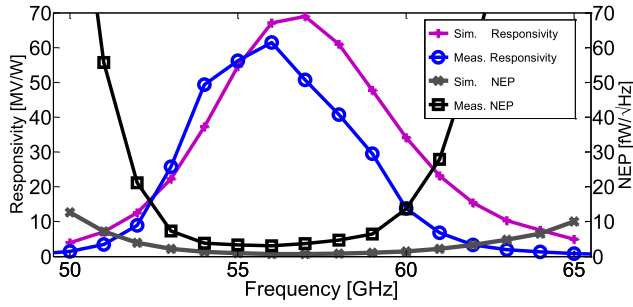


Fig. 17. Measured and simulated NEP and responsivity across frequency with a detector bias voltage of 680 mV, which correspond with the planes cutting through Figs. 14. and 15.

The listed LNA gain of 21 dB was measured on a 50- $\Omega$  termination. The deduced gain of the LNA when terminated by the detector is around 28 dB. The low noise figure of 5.3 dB compared with other LNAs originates from the reduced operating frequency. However, (14) allows approximate noise figure comparison across frequency. When  $f > f_T/\sqrt{\beta}$  ( $\sim 14$  GHz for this design), the NFmin tends to increase 10 dB/Dec with increasing frequency [30]. Implying that there would be a 3 dB/Octave increase or in this case a 3-dB and 4.5-dB increase at 110 and 150 GHz, respectively, provided the HBTs still exhibits gain. The simple three-stage design allowed us to operate on 18-mA dc current, an advantage that is, however, largely negated, in terms of power by the 2.5-V supply voltage. The bandwidth achieved with two-stage LNA, stated in a percentage of the carrier, is comparable to some of the designs using three to five stages. This results from offsetting frequency transfers gain peaks in the LNA and the use of the high impedance (i.e., voltage) transfer between the LNA and detector. The reported responsivity is not the highest, but this metric should always be to what can be achieved in terms of NEP with which this simple design compares quite favorably with others published.

## V. CONCLUSION

This paper presents the analysis, design, and characterization of a 56-GHz detector-limited total-power radiometer front-end integrated into a 0.25- $\mu\text{m}$  SiGe:C BiCMOS process. The analysis illustrates that for small temperature resolution, one requires the front end to have high gain, a broad RF bandwidth, and an efficient power-to-voltage conversion, while simultaneously providing a low noise figure and producing a minimum amount of white- and flicker noise at the output. Employing the guidelines from the presented analysis, a radiometer composed of two cascode stage LNA and a square-law detector is presented. The LNA achieves a deduced gain of 28 dB across a 6-dB bandwidth when terminated by the high input impedance of the detector and measurements on a 50- $\Omega$  show a noise figure of 5.3 dB. The detector achieves both low NEP numbers and flicker noise corner by employing a large area, high resistive value p-type poly-silicon load resistor in combination with a minimum size HBT. Measurement results on the test chip prototype front end showed a peak responsivity of 152 mV/W at 56 GHz and a 720 mV-bias voltage for the detector. The minimum NEP of 3.2 fF/ $\sqrt{\text{Hz}}$  is, however, found

at the same frequency and a detector bias of 680 mV. This low NEP results from the 194-nV/ $\sqrt{\text{Hz}}$  white noise level beyond the 30-Hz  $1/f$ -corner frequency and 61-MV/W responsivity found at this bias.

## ACKNOWLEDGMENT

The authors would like to thank NXP semiconductors for providing technology access.

## REFERENCES

- [1] J. A. Nanzer, *Microwave and Millimeter-Wave Remote Sensing for Security Applications*. Norwood, MA, USA: Artech House, 2012.
- [2] L. Yujiri, M. Shoucri, and P. Moffa, "Passive millimeter-wave imaging," *IEEE Microw. Mag.*, vol. 4, no. 3, pp. 39–50, Sep. 2004.
- [3] A. Tang, Q. J. Gu, and M. C. F. Chang, "CMOS receivers for active and passive mm-wave imaging," *IEEE Commun. Mag.*, vol. 49, no. 10, pp. 190–198, Oct. 2011.
- [4] B. H. S. Gharavi, *Ultra High-Speed CMOS Circuits*. New York, NY, USA: Springer, 2012.
- [5] J. D. Cressler, *Fabrication of SiGe HBT BiCMOS Technology*. Boca Raton, FL, USA: CRC Press, 2007.
- [6] J. W. May and G. M. Rebeiz, "Design and characterization of W-band SiGe RFICs for passive millimeter-wave imaging," *IEEE Trans. Microw. Theory Techn.*, vol. 58, no. 5, pp. 1420–1430, May 2010.
- [7] A. Tomkins, P. Garcia, and S. P. Voinigescu, "A passive W-band imaging receiver in 65-nm bulk CMOS," *IEEE J. Solid-State Circuits*, vol. 45, no. 10, pp. 1981–1991, Oct. 2010.
- [8] L. Zhou, C.-C. Wang, Z. Chen, and P. Heydari, "A W-band CMOS receiver chipset for millimeter-wave radiometer systems," *IEEE J. Solid-State Circuits*, vol. 46, no. 2, pp. 378–391, Feb. 2011.
- [9] Q. J. Gu, Z. Xu, A. Tang, and M. Chang, "A D-band passive imager in 65 nm CMOS," *IEEE Microw. Wireless Compon. Lett.*, vol. 22, no. 5, pp. 263–265, May 2012.
- [10] Q. J. Gu *et al.*, "A CMOS integrated W-band passive imager," *IEEE Trans. Circuits Syst. II, Exp. Briefs*, vol. 59, no. 11, pp. 736–740, Nov. 2012.
- [11] L. Gilreath, V. Jain, and P. Heydari, "Design and analysis of a W-band SiGe direct-detection-based passive imaging receiver," *IEEE J. Solid-State Circuits*, vol. 46, no. 10, pp. 2240–2252, Oct. 2011.
- [12] E. Dacquay *et al.*, "D-band total power radiometer performance optimization in a SiGe HBT technology," *IEEE Trans. Microw. Theory Techn.*, vol. 60, no. 3, pp. 813–826, Mar. 2012.
- [13] Z. Chen, C.-C. Wang, H.-C. Yao, and P. Heydari, "A BiCMOS W-band 2 $\times$ 2 focal-plane array with on-chip antenna," *IEEE J. Solid-State Circuits*, vol. 47, no. 10, pp. 2355–2371, Oct. 2012.
- [14] F. Caster, L. Gilreath, S. Pan, Z. Wang, F. Capolino, and P. Heydari, "Design and analysis of a W-band 9-element imaging array receiver using spatial-overlapping super-pixels in silicon," *IEEE J. Solid-State Circuits*, vol. 49, no. 6, pp. 1317–1332, Jun. 2014.
- [15] E. Shumaker and D. Elad, "Analog read-out integrated W-band Dicke-radiometer in 0.13 $\mu\text{m}$  SiGe design and characterization of W-band radiometer RFIC intended for FPA imager," in *Proc. Microw. Conf. (EuMC)*, Rome, Italy, Sep. 2014, pp. 1130–1133.
- [16] R. Yishay, E. Shumaker, and D. Elad, "Key components of a D-band Dicke-radiometer in 90 nm SiGe BiCMOS technology," in *Proc. Microw. Integr. Circuits Conf. (EuMIC)*, Paris, France, May 2015, pp. 176–179.
- [17] X. Bi, M. Arasu, Y. Zhu, and M. Je, "A low switching-loss W-band radiometer utilizing a single-pole-double-throw distributed amplifier in 0.13- $\mu\text{m}$  SiGe BiCMOS," *IEEE Trans. Microw. Theory Techn.*, vol. 64, no. 1, pp. 226–238, Jan. 2016.
- [18] T. Kanar and G. M. Rebeiz, "A low-power 136-GHz SiGe total power radiometer with NETD of 0.25 K," *IEEE Trans. Microw. Theory Techn.*, vol. 64, no. 3, pp. 906–914, Mar. 2016.
- [19] R. Dicke, "The measurement of thermal radiation at microwave frequencies," *Rev. Sci. Instrum.*, vol. 17, no. 7, pp. 268–275, 1946.
- [20] A. C. Ulusoy, R. L. Schmid, C. Coen, and J. D. Cressler, "A switchable-core SiGe HBT low-noise amplifier for millimeter-wave radiometer applications," in *Proc. IEEE 14th Topical Meeting Silicon Monolithic Integr. Circuits Rf Syst.*, Newport Beach, CA, USA, Jan. 2014, pp. 22–24.
- [21] J. Lesurf, *Information and Measurement*, 2nd ed. Boca Raton, FL, USA: CRC Press, 2001.

- [22] M. E. Tiuri, "Radio astronomy receivers," *IEEE Trans. Military Electron.*, vol. 8, no. 3, pp. 264–272, Jul. 1964.
- [23] T. L. Wilson, K. Rohlf, and S. Hüttemeister, *Tools of Radio Astronomy*. Berlin, Germany: Springer, 2009.
- [24] G. Evans and C. W. McLeish, *RF Radiometer Handbook*. Dedham, MA, USA: Artech House, 1977.
- [25] E. J. McDowell, J. Ren, and C. Yang, "Fundamental sensitivity limit imposed by dark  $1/f$  noise in the low optical signal detection regime," *Opt. Exp.*, vol. 16, no. 10, pp. 6822–6832, 2008.
- [26] D. A. Thompson, R. L. Rogers, and J. H. Davis, "Temperature compensation of total power radiometers," *IEEE Trans. Microw. Theory Techn.*, vol. 51, no. 10, pp. 2073–2078, Oct. 2003.
- [27] S. Diebold, E. Weissbrodt, H. Massler, A. Leuther, A. Tessmann, and I. Kallfass, "A W-band monolithic integrated active hot and cold noise source," *IEEE Trans. Microw. Theory Techn.*, vol. 62, no. 3, pp. 623–630, Mar. 2014.
- [28] W. D. van Noort *et al.*, "BiCMOS technology improvements for microwave application," in *Proc. Bipolar/BiCMOS Circuits Technol. Meeting*, Monterey, CA, USA, Sep. 2008, pp. 93–96.
- [29] A. B. Smolders, H. Gul, E. V. D. Heijden, P. Gamand, and M. Geurts, "BiCMOS high-performance ICs: From DC to mm-wave," in *Proc. Bipolar/BiCMOS Circuits Technol. Meeting*, Capri, Italy, Oct. 2009, pp. 115–122.
- [30] P. H. C. Magnée *et al.*, "SiGe:C profile optimization for low noise performance," in *Proc. IEEE Bipolar/BiCMOS Circuits Technol. Meeting*, Atlanta, GA, USA, Oct. 2011, pp. 166–169.
- [31] J. Bergervoet, D. M. W. Leenaerts, G. W. D. Jong, E. V. D. Heijden, J. W. Lobeek, and A. Simin, "A 1.95 GHz sub-1 dB NF, +40 dBm OIP3 WCDMA LNA module," *IEEE J. Solid-State Circuits*, vol. 47, no. 7, pp. 1672–1680, Jul. 2012.
- [32] G. Niu, A. Joseph, and D. Hareme, "Noise-gain tradeoff in RF SiGe HBTs," in *Proc. Topical Meeting Silicon Monolithic Integr. Circuits RF Syst.*, Ann Arbor, MI, USA, Apr. 2001, pp. 1445–1451.
- [33] G. Manganaro and D. M. Leenaerts, *Advances in Analog and RF IC Design for Wireless Communication Systems*, 1st ed. Waltham, MA, USA: Elsevier, 2013.
- [34] D. K. Shaeffer and T. H. Lee, "A 1.5-V, 1.5-GHz CMOS low noise amplifier," *IEEE J. Solid-State Circuits*, vol. 32, no. 5, pp. 745–759, May 1997.
- [35] R. Sananes and E. Socher, "52–75 GHz wideband low-noise amplifier in 90 nm CMOS technology," *Electron. Lett.*, vol. 48, no. 2, pp. 71–72, 2012.
- [36] T. Yao *et al.*, "Algorithmic design of CMOS LNAs and PAs for 60-GHz radio," *IEEE J. Solid-State Circuits*, vol. 42, no. 5, pp. 1044–1057, May 2007.
- [37] J. R. Long and M. A. Copeland, "The modeling, characterization, and design of monolithic inductors for silicon RF IC's," *IEEE J. Solid-State Circuits*, vol. 32, no. 3, pp. 357–369, Mar. 1997.
- [38] J. Shi, K. Kang, Y. Z. Xiong, J. Brinkhoff, F. Lin, and X. J. Yuan, "Millimeter-wave passives in 45-nm digital CMOS," *IEEE Electron Device Lett.*, vol. 31, no. 10, pp. 1080–1082, Oct. 2010.
- [39] R. Al Hadi, J. Grzyb, B. Heinemann, and U. R. Pfeiffer, "A terahertz detector array in a SiGe HBT technology," *IEEE J. Solid-State Circuits*, vol. 48, no. 9, pp. 2002–2010, Sep. 2013.
- [40] E. S. Malotaux and M. Spirito, "Characterization of broadband low-NEP SiGe square-law detectors for mm-wave passive imaging," in *IEEE MTT-S Int. Microw. Symp. Dig.*, San Francisco, CA, USA, Sep. 2016, pp. 1–4.
- [41] P. R. Gray, P. Hurst, S. Lewis, and R. Meyer, *Analysis and Design of Analog Integrated Circuits*, 4th ed. New York, NY, USA: Wiley, 2001.
- [42] R. Brederlow, W. Weber, C. Dahl, D. Schmitt-Landsiedel, and R. Thewes, "Low-frequency noise of integrated polysilicon resistors," *IEEE Trans. Electron Devices*, vol. 48, no. 6, pp. 1180–1187, Jun. 2001.
- [43] M. Uzunkol, O. D. Gurbuz, F. Golcuk, and G. M. Rebeiz, "A 0.32 THz SiGe  $4 \times 4$  imaging array using high-efficiency on-chip antennas," *IEEE J. Solid-State Circuits*, vol. 48, no. 9, pp. 2056–2066, Sep. 2013.
- [44] L. Galatro, S. Galbano, A. Santaniello, and M. Spirito, "Power control for S-parameters and large signal characterization at (sub)-mmWave frequencies," in *Proc. 85th Microw. Meas. Conf. (ARFTG)*, Phoenix, AZ, USA, May 2015, pp. 1–4.



**Satoshi Malotaux** (S'14) received the M.Sc. degree in electrical engineering from the Delft University of Technology, Delft, The Netherlands, in 2013, where he is currently pursuing the Ph.D. degree in electrical engineering.

His current research interests include millimeter wave integrated circuit design and mm-wave and sub-mm-wave imaging systems.



**Masoud Babaie** (S'12–M'16) received the B.Sc. (with highest Hons.) degree in electrical engineering from the Amirkabir University of Technology, Tehran, Iran, in 2004, the M.Sc. degree in electrical engineering from the Sharif University of Technology, Tehran, in 2006, and the Ph.D. (cum laude) degree from the Delft University of Technology, Delft, The Netherlands, in 2016.

In 2006, he joined the Kavoshcom Research and Development Group, Tehran, where he was involved in designing tactical communication systems and was a CTO from 2009 to 2011. From 2013 to 2015, he was consulting for the RF Group of Taiwan Semiconductor Manufacturing Company, Hsinchu, Taiwan, where he was involved in designing 28-nm all-digital phase-locked loop and Bluetooth low-energy transceiver chips. From 2014 to 2015, he was a Visiting Scholar Researcher with the Berkeley Wireless Research Center, Berkeley, CA, USA, with the Group of Prof. A. Niknejad. In 2016, he joined the Delft University of Technology as an Assistant Professor. His current research interests include analog and RF/millimeter-wave integrated circuits and systems for wireless communications, and cryogenic electronics for quantum computation.

Dr. Babaie was a recipient of the 2015–2016 IEEE Solid-State Circuits Society Pre-Doctoral Achievement Award. He serves as a reviewer for the IEEE Journal of Solid-State Circuits.



**Marco Spirito** (S'01–M'08) received the M.Sc. degree (cum laude) in electrical engineering from the University of Naples Federico II, Naples, Italy, in 2000, and the Ph.D. degree from the Delft University of Technology, Delft, The Netherlands, in 2006.

In 2008, he joined the Electronics Research Laboratory, Delft University of Technology, as an Assistant Professor, where he has been an Associate Professor since 2013. He was one of the co-founders of the startup Anteverta-MW. His current research interests include the characterization of highly efficient and linear power amplifiers, the development of advanced characterization setups for microwave, millimeter and submillimeter waves, and the integration of millimeter-wave sensing systems.